Altshuler-Aronov-Spivak interference of one-dimensional helical edge states in $MoTe_2$

Zhen-Cun Pan,[1] Chun-Guang Chu,[1] Jing-Jing Chen,[2,*] An-Qi Wang,[1] Zhen-Bing Tan,[2] Wen-Zheng Xu,[1] Jun Xu,[3] Xiu-Mei Ma,[3] Da-Peng Yu,[2] and Zhi-Min Liao[1,†]

[1]*State Key Laboratory for Mesoscopic Physics and Frontiers Science Center for Nano-optoelectronics, School of Physics, Peking University, Beijing 100871, China*

[2]*Shenzhen Institute for Quantum Science and Engineering, Southern University of Science and Technology, Shenzhen 518055, China and International Quantum Academy, Shenzhen 518055, China*

[3]*Electron Microscopy Laboratory, School of Physics, Peking University, Beijing 100871, China*

(Received 9 September 2022; accepted 4 January 2023; published 12 January 2023)

Recent theories predicted that 1T′-$MoTe_2$ is a higher-order topological insulator (HOTI) exhibiting one-dimensional (1D) conducting edge states, and that T_d-$MoTe_2$ becomes a HOTI with broken inversion symmetry under strain or lattice distortion. Here, we report the transport evidence for 1D helical edge states in $MoTe_2$ thin flakes. Under an in-plane magnetic field perpendicular to the current, Altshuler-Aronov-Spivak interference of edge states is observed, in which the oscillating period corresponding to magnetic flux $h/2e$ agrees with the lateral cross-sectional area. The absence of Aharonov-Bohm interference stems from the helical nature of the edge states. Temperature evolution of the fast Fourier transform amplitude is further obtained, indicating the quasiballistic transport mode. Our work deepens the understanding of higher-order topological properties of $MoTe_2$, paving the way for further topological electronics.

DOI: 10.1103/PhysRevB.107.045411

I. INTRODUCTION

Transition metal dichalcogenides (TMDCs) have broadly studied in recent years as a playground for emerging quantum effects benefiting from their exotic electronic structures [1–4]. As one of them, molybdenum ditelluride ($MoTe_2$) has been predicted as a two-dimensional (2D) topological insulator (TI) in its monolayer 1T′ phase with inverted chalcogen p and transition metal d bands [5], and as a type-II Weyl semimetal in its T_d phase [6–8]. Recently, the concept of topology in condensed matter has been broadened above the $\mathbb{Z}_2$ parity paradigm [9,10]. By analyzing the parity of the "elementary" band representations of insulators [11,12], a $\mathbb{Z}_4$ index should be adopted in the higher-order topological insulator (HOTI) phase scenario [13–15]. Based on this $\mathbb{Z}_4$ index and Wilson loop methods, the topology of XTe_2 (X = W, Mo) electronic structure has been restudied and identified within the higher-order regime, i.e., the HOTI phase, in $MoTe_2$ with both 1T′ and T_d phases [16–18]. Signatures of the fast oscillation mode of the critical current of edge supercurrent in $MoTe_2$ bulk materials have been reported [19].

Apart from resolving edge supercurrents, Aharonov-Bohm (AB) and Altshuler-Aronov-Spivak (AAS) interference in normal states are effective and convincing methods to manifest the surface or edge transport in carbon nanotubes [20], topological insulators [21–24], and Dirac/Weyl semimetals [25,26]. Previous works have focused on nanowire systems, taking advantage of their large surface to volume ratio to enhance surface conduction contribution [27]. When applying a magnetic field B along the nanowire axis, circling carriers around the perimeter accumulate a $2\pi\Phi/\Phi_0$ phase, where $\Phi = BS$ is the magnetic flux threading through the cross-sectional area S, and $\Phi_0 = h/e$ is the magnetic flux quantum, causing AB oscillation with a h/e period in magnetoconductance (MC) [28]. In the presence of pairs of time-reversal paths, the magnetic flux is doubled, thus causing the AAS oscillations with the $h/2e$ period. The possibility of the AB or AAS effect in three dimensions (3D) based on higher-order topological edge states is predicted as a natural continuation [29]. Under a perpendicular magnetic field, loops formed by propagating one-dimensional (1D) edge states acquire a quantum phase due to AB or AAS interference and exhibit periodic oscillation in MC.

In this work, we report the AAS interference of 1D helical edge states in $MoTe_2$ thin flakes. Weak antilocalization (WAL) is observed under an out of plane magnetic field, exhibiting the transport features of 2D surface states in $MoTe_2$. Negative magnetoresistance (NMR) is obtained under an in-plane magnetic field with a parallel component along the current direction, which is attributed to the Adler-Bell-Jackiw chiral anomaly mechanism [30]. When applying an in-plane perpendicular magnetic field, oscillations in MC are observed, of which the fast Fourier transform (FFT) corroborates its AAS interference frequency, in agreement with the lateral cross-sectional area. Moreover, the temperature dependence of the FFT amplitude offers evidence of a quasiballistic transport channel.

II. EXPERIMENTAL METHOD

The $MoTe_2$ thin flakes were first mechanically exfoliated and then transferred onto a silicon substrate with a 285 nm

*chenjj3@sustech.edu.cn
†liaozm@pku.edu.cn

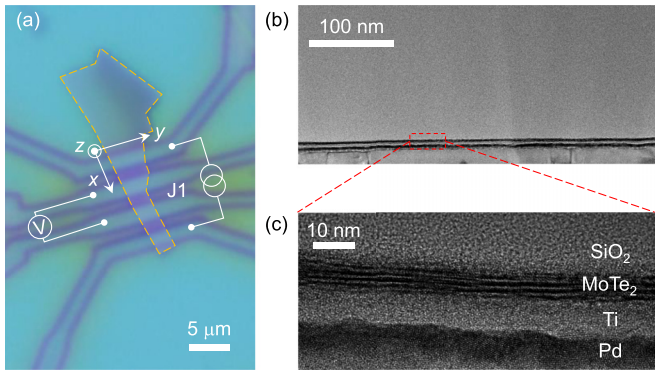

FIG. 1. Characterization of the $MoTe_2$ device. (a) An optical image of the device. The $MoTe_2$ thin flake is denoted by the yellow dashed lines. Junction 1 is denoted by J1. Four-probe measurement configuration is illustrated. (b) The TEM image of the cross section of the device. (c) Enlarged TEM image of the region denoted by the red dashed box in (b). The $MoTe_2$ thin flake is about 7 nm thick.

SiO_2 layer. The Ti/Pd electrodes were defined by electron beam lithography and grown by electron beam evaporation processes. Figure 1(a) shows the optical image of the $MoTe_2$ device. The $MoTe_2$ thin flake is denoted by the yellow dashed lines. Junction 1 is denoted by J1. The four-probe method is utilized to perform transport measurements, as shown schematically in Fig. 1(a). A standard low-frequency lock-in technique is used to measure the conductance in a commercial dilution refrigerator with a base temperature of 10 mK. The channel length L of junction 1 is about 1.3 μm. Figure 1(b) shows the transmission electron microscope (TEM) image of the cross section of the $MoTe_2$ device fabricated by the focused ion beam technique. The enlarged region denoted by the red dashed box in Fig. 1(b) is shown in Fig. 1(c). The layered structure of $MoTe_2$ and electrodes Ti, Pd is clearly observed. The thickness t of the $MoTe_2$ thin flake is about 7 nm.

III. RESULTS AND DISCUSSION

An out of plane magnetic field B_z is applied to study the MC of J1, and the results at different temperatures are presented in Fig. 2(a), where $\Delta G(B_z) = G(B_z)–G(0)$. Sharp conductance peaks near zero magnetic field at different temperatures are clearly seen. Similar effects were reported in surface states of TIs [21,31–33] and TMDCs [34,35]. Considering the strong spin-orbit coupling in $MoTe_2$ [36], WAL causes a negative MC. The WAL behavior in $MoTe_2$ is further quantified by the Hikami-Larkin-Nagaoka (HLN) model [37],

$$\Delta G(B) = -\alpha \frac{e^2}{\pi h}\left[\ln\left(\frac{\hbar}{4eBL_\phi^2}\right) - \psi\left(\frac{\hbar}{4eBL_\phi^2}+\frac{1}{2}\right)\right], \quad (1)$$

where $\psi(x)$ is the digamma function and L_ϕ is the phase coherence length. Conductance correction $\Delta G(B_z)$ is fitted under a low magnetic field by the HLN formula (1), as depicted by the dashed curves in Fig. 2(a). Temperature evolution of the fitting parameters L_ϕ and α up to 1.46 K is shown in Fig. 2(b). The coherence length L_ϕ is extracted to be smaller than 300 nm at low temperatures, indicating the diffusive transport of the surface states in $MoTe_2$ (channel length $L \sim 1.3$ μm). The temperature dependence of L_ϕ obeys an appropriate $T^{-0.51}$ power law [denoted by the black curve in Fig. 2(b)], which is consistent with theories of 2D electron systems with nonexisting inelastic phonon scattering, where $T^{-1/2}$ dependence was commonly observed in TI nanoribbons [32,38] in previous reports in the literature. The prefactor α is fitted to be around -0.5 over the temperature range, consistent with the theoretical value for a system with strong spin-orbit interaction without magnetic scattering [37].

Magnetoresistance (MR) is further studied by applying an in-plane magnetic field. A schematic of magnetic field B direction is presented in Fig. 3(a), where φ is defined as the angle between B and the current direction. φ-dependent MR is shown in Fig. 3(b). For $\varphi = 90°$, the resistance increases with a superimposed oscillation from $B = 0.3$ to 1.0 T. As B gradually rotates towards the longitudinal direction

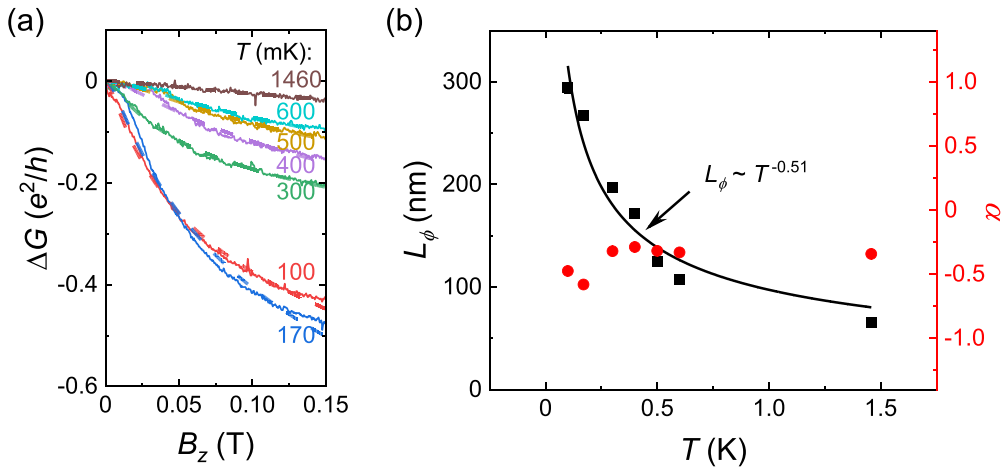

FIG. 2. Weak antilocalization (WAL) under out of plane magnetic field B_z in junction 1. (a) Conductance ΔG as a function of B_z at different temperatures. $\Delta G = G(B_z)–G(0)$. The conductance correction due to WAL is fitted with the HLN model, as shown by the corresponding dashed curves. (b) Temperature dependence of the phase coherence length L_ϕ (left axis, black symbols) and prefactor α (right axis, red symbols) extracted from the fittings in (a). The fitted power law is denoted by the black curve.

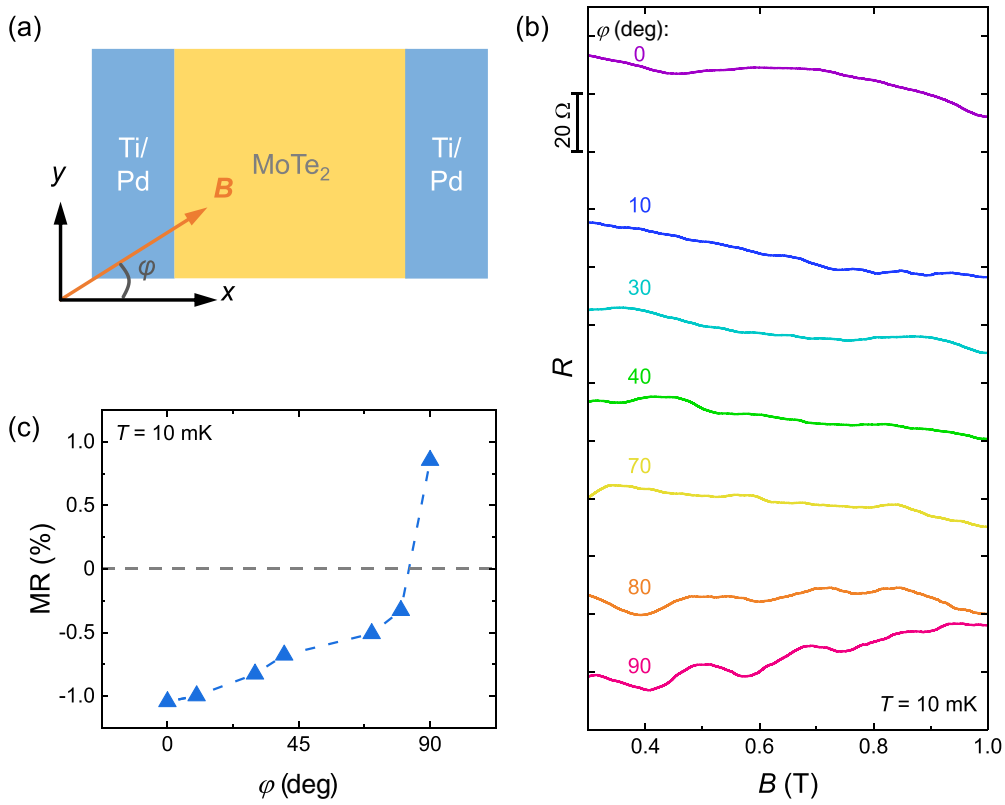

FIG. 3. Negative magnetoresistance (NMR) under an in-plane magnetic field with a parallel component along the current direction in junction 1. (a) Schematic of the orientation of the in-plane magnetic field B. The angle between B and the x direction is defined as φ. (b) Resistance as a function of B at several angles φ at $T = 10$ mK. Traces are shifted vertically for clarity with the offset of 35 Ω. (c) Angle dependence of MR, where MR $= [R(B = 1\,\mathrm{T})–R(B = 0.3\,\mathrm{T})]/R(B = 0.3\,\mathrm{T})$.

(x axis), resistance decreases at a higher magnetic field. The transition is plotted more apparently in Fig. 3(c), in which MR is defined as $[R(B = 1\,\mathrm{T})–R(B = 0.3\,\mathrm{T})]/R(B = 0.3\,\mathrm{T})$. NMR is obtained at all directions except the perpendicular field ($\varphi = 90°$). Considering the first-order structural phase transition from the 1T′ to the T_d phase in $MoTe_2$ at $T \approx 260$ K [39], the type-II Weyl semimetal property may contribute to NMR behavior [6–8]. Under electric and magnetic fields, the continuity equation of right- and left-handed Weyl nodes takes the form of $\nabla \cdot j^{R,L} + \partial_t \rho^{R,L} = \pm \frac{e^3}{4\pi^2\hbar^2 c} \boldsymbol{E} \cdot \boldsymbol{B}$ [40], resulting in a nonconserving chiral charge if $\boldsymbol{E} \cdot \boldsymbol{B} \neq 0$. Chiral anomaly thus induces the charge pumping between nodes of opposite chirality at a rate proportional to $\boldsymbol{E} \cdot \boldsymbol{B}$, giving rise to a conductivity $\sigma^{\mathrm{chiral}} = \frac{e^2}{4\pi^2\hbar c} \frac{v}{c} \frac{[eB\cos(\varphi)v]^2}{E_F^2} \tau$, resulting in the NMR, where v is the Fermi velocity near the Weyl nodes, E_F is the chemical potential, and τ is the internode scattering time [41]. With increasing parallel component $B\cos(\varphi)$, the amplitude of NMR increases monotonically as $\boldsymbol{B}$ tilts towards $\boldsymbol{E}$ [Fig. 3(c)], which is consistent with the chiral current mechanism.

Under an in-plane perpendicular field B_y [$\varphi = 90°$ as defined in Fig. 3(a)], the AAS interference is observed and presented in Fig. 4. After subtracting a smooth background, clear oscillations of $\delta G(B_y)$ at different temperatures are obtained [Fig. 4(a)]. To extract the oscillation frequency, we take advantage of the FFT. Figure 4(b) manifests the FFT spectrum at $T = 50$ mK, indicating a major frequency of $4.76\,\mathrm{T}^{-1}$ (period: 0.21 T). For the AAS interference with $h/2e$ frequency, this period corresponds to an area of $9.8 \times 10^{-15}\,\mathrm{m}^2$. Considering that the thickness t of the $MoTe_2$ flake is ∼ 7 nm [Fig. 1(c)], the obtained lateral cross-sectional area is consistent with the channel length L(∼ 1.3 μm), which indicates that there are conductive 1D channels along the hinge, as illustrated schematically in Fig. 4(c). The observed AAS interference is reproducible in junction 2 (see Fig. 5 and Appendix A). When applying an out of plane magnetic field B_z, however, clear periodic oscillations are absent (see Fig. 6 and Appendix B). For edge states to form interference loops under B_z, electrons must cross the width direction of the junction, resulting in much longer paths that probably exceed the coherence length of the edge states. Also, the magnetoresistance of the conducting top and bottom surface states contributes a notable background, which may dissimulate the interference signals.

As for the in-plane perpendicular B_y field, the bulk and side surface states are gapped out to a large extent due to the quantum confinement effect, considering the thin flake's thickness (∼7 nm) compared to the mean-free path of T_d−$MoTe_2$ (∼100 nm) [42]. Thus, coherent quantum interference of 1D edge states is highlighted. As for the absence of AB interference, it indicates the helical nature of the edge states. For edge states located at the same sidewall, the two right-propagating paths on the top and bottom edges could not form AB interference since they carry opposite spin [shown by red and black arrows in Fig. 4(c)].

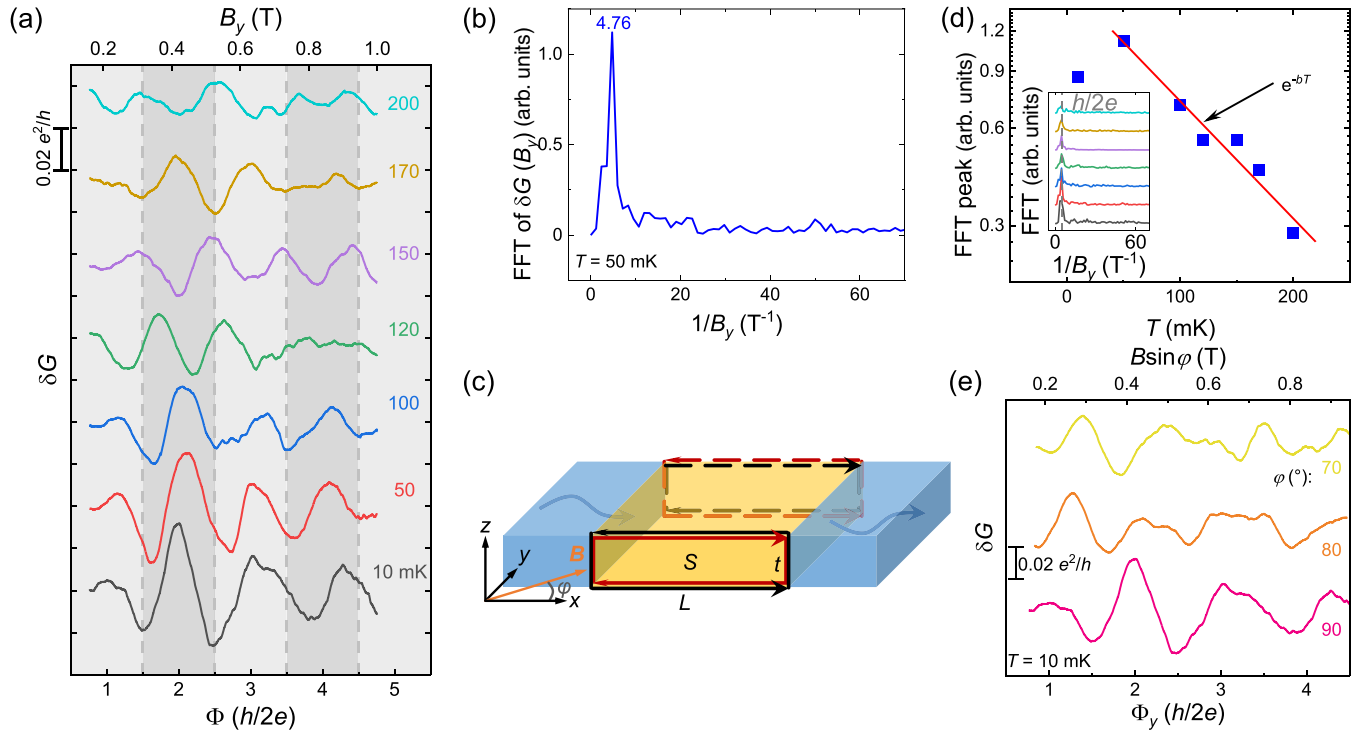

FIG. 4. Altshuler–Aronov–Spivak (AAS) interference of 1D helical edge states in junction 1. (a) Conductance as a function of magnetic flux Φ (converted from in-plane perpendicular magnetic field B_y) at various temperatures. δG is obtained by subtracting a smooth background. Traces are shifted for clarity. (b) Fast Fourier transform (FFT) of δG (B_y) at $T = 50$ mK. The major peak located at 4.76 T^{-1} corresponds to $h/2e$ periodic oscillation. (c) Schematic of the helical edge states. Helical edge states with opposite spin propagating in opposite directions are illustrated by red and black arrows, respectively. (d) Temperature evolution of FFT peak amplitude as a semilog plot. The fitted exponential law is shown as the red line. Inset: FFT of $\delta G(B_y)$ for each temperature [colors correspond to (a)], showing the robust $h/2e$ period. (e) δG as a function of the perpendicular component of magnetic flux Φ_y (associated with $B\sin\varphi$) at different φ at $T = 10$ mK. Curves are shifted for visibility.

To further demonstrate the periodicity, we convert magnetic field B_y into magnetic flux Φ in Fig. 4(a). At 10–100 mK, peaks are located at the integer multiples of $h/2e$. Intriguingly, conductance dips at the integer multiples of $h/2e$ happen at $T = 150$ mK, indicating a π phase shift. At $T = 120$ mK, the phase shift is approximate $\pi/2$, which is considered an intermediate state during the transition. Two subsequent transitions occur at 170 and 200 mK, respectively. Previously the π phase transition in quantum interference was usually obtained by tuning the Fermi level of TI [43] or Dirac semimetal [26] nanowire systems. The sensitivity of the quantum phase (0 or π) to temperature here in $MoTe_2$ may be attributed to dephasing by disorder or influence on Fermi energy by thermal fluctuation [22,23], which was also observed in TI nanoribbons [33]. The FFT spectrum of $\delta G(B_y)$ at each temperature is plotted in the inset of Fig. 4(d), indicating the robust dominant $h/2e$ frequency. The temperature evolution of the FFT peak amplitude at $h/2e$ frequency is presented in Fig. 4(d). The linear fit in a semilog plot gives an exponentially decaying behavior, i.e., FFT amplitude $\sim e^{-bT}$, which indicates the 1D quasiballistic edge channel, as reported in TI [33,44] and Dirac semimetals [26]. The deviation at $T < 50$ mK is probably due to negligible influence of thermal broadening on the electron wave packets [45]. Another possible reason is that the carrier temperature may differ from the lattice temperature, resulting in an error at 10 mK. To further verify the edge interference picture, δG as a function of magnetic flux at several magnetic field directions φ is measured [φ defined in Figs. 3(a) and 4(c)]. As shown in Fig. 4(e), the horizontal axis is scaled into the perpendicular component Φ_y and $B\sin\varphi$. It is observed that the oscillation peaks and dips are approximately aligned for $\varphi = 80°$ and 90°, indicating the dominance of magnetic flux threading through the lateral side of the $MoTe_2$ flake, which provides additional evidence of the edge interference. For $\varphi = 70°$, misalignment and peak splitting occurs, which is attributed to possible time-reversal symmetry breaking effect induced by the longitudinal field component $B\cos\varphi$, thus suppressing the edge interference [46].

IV. CONCLUSIONS

In summary, we have demonstrated the transport properties of the 1D higher-order helical edge states in $MoTe_2$ by uncovering the AAS interference. Under an in-plane magnetic field perpendicular to the current, conductance oscillations with a $h/2e$ flux period are observed at low temperatures. Moreover, it is found that the AB effect is absent, which is attributed to the decoherence of electrons moving along the same direction on two different edges, resulting from the helical edge states carrying opposite spin. Further, the temperature dependence of AAS interference suggests the 1D quasiballistic edge states. Our work manifests the quantum interference properties of higher-order topological states in $MoTe_2$, paving the way for further topological and spintronic devices.

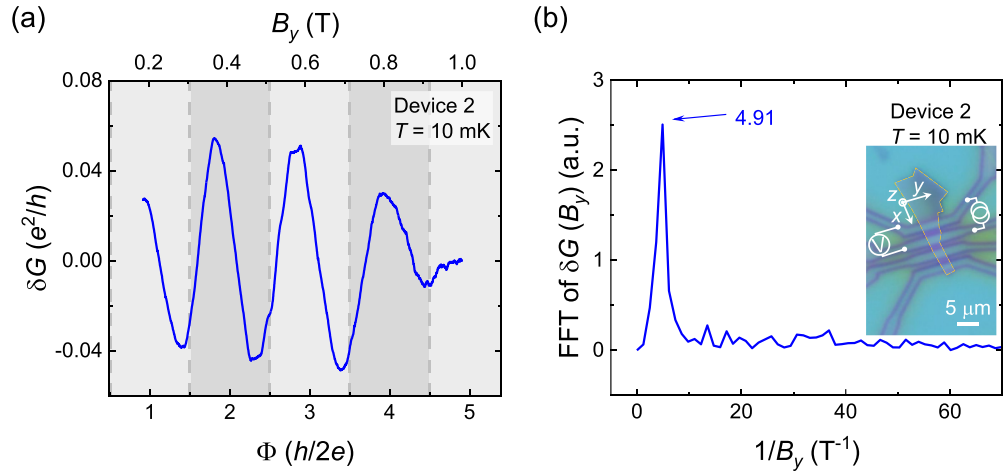

FIG. 5. AAS interference in junction 2. (a) MC at 10 mK in junction 2. A smooth background has been subtracted to obtain δG. (b) FFT of $\delta G(B_y)$ in (a). The major peak at 4.91 T^{-1} reveals the AAS oscillation with the $h/2e$ period. Inset: optical image and measurement configuration of junction 2.

ACKNOWLEDGMENTS

This work was supported by the National Key Research and Development Program of China (Grant No. 2018YFA0703703) and the National Natural Science Foundation of China (Grants No. 91964201 and No. 61825401).

APPENDIX A: AAS INTERFERENCE IN JUNCTION 2

Junction 2 with similar geometric dimensions ($t \sim 7$ nm, $L \sim 1.3$ μm) has been studied. A pseudo-four-probe measurement method is employed to perform the transport measurements [inset of Fig. 5(b)]. Under an in-plane perpendicular magnetic field B_y, the AAS interference of $MoTe_2$ is

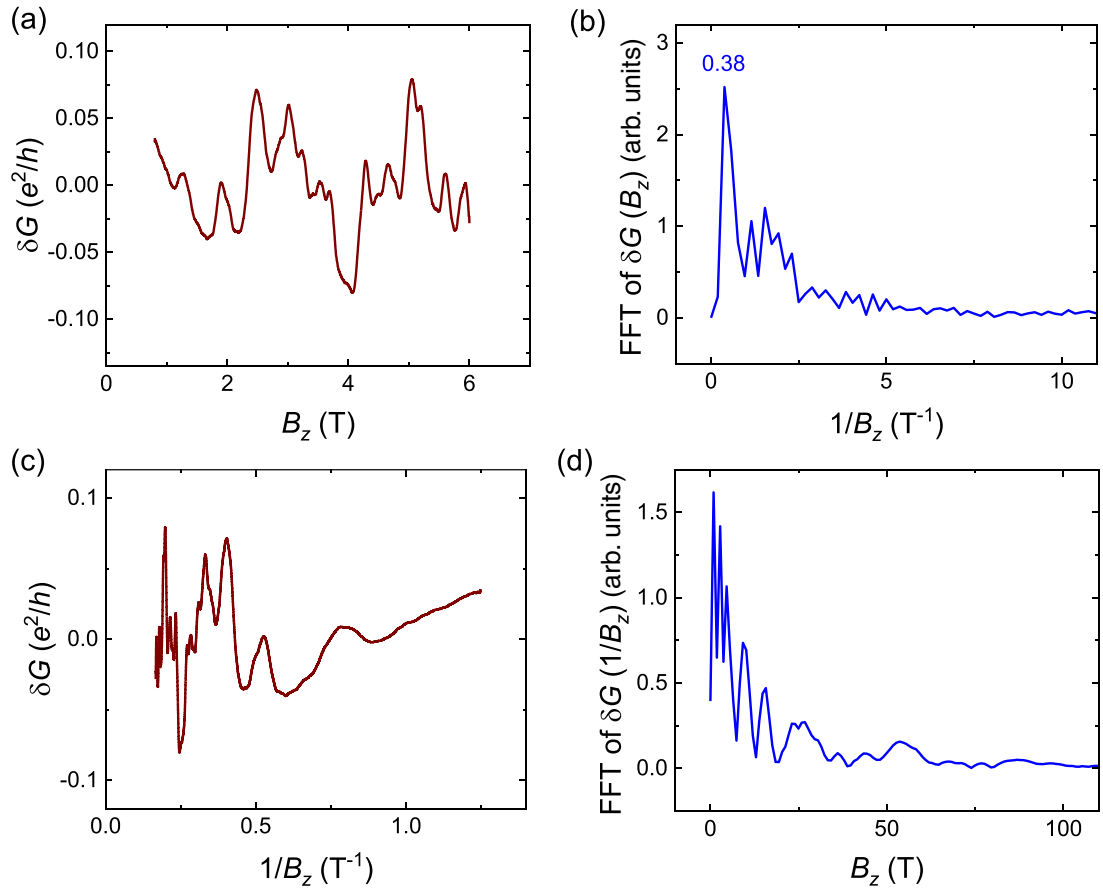

FIG. 6. Magnetoconductance under an out of plane magnetic field in junction 1. (a) δG versus B_z. A smooth background is subtracted. (b) FFT of (a). The major peak locates at 0.38 T^{-1}. (c) δG versus $1/B_z$. (d) FFT of (c).

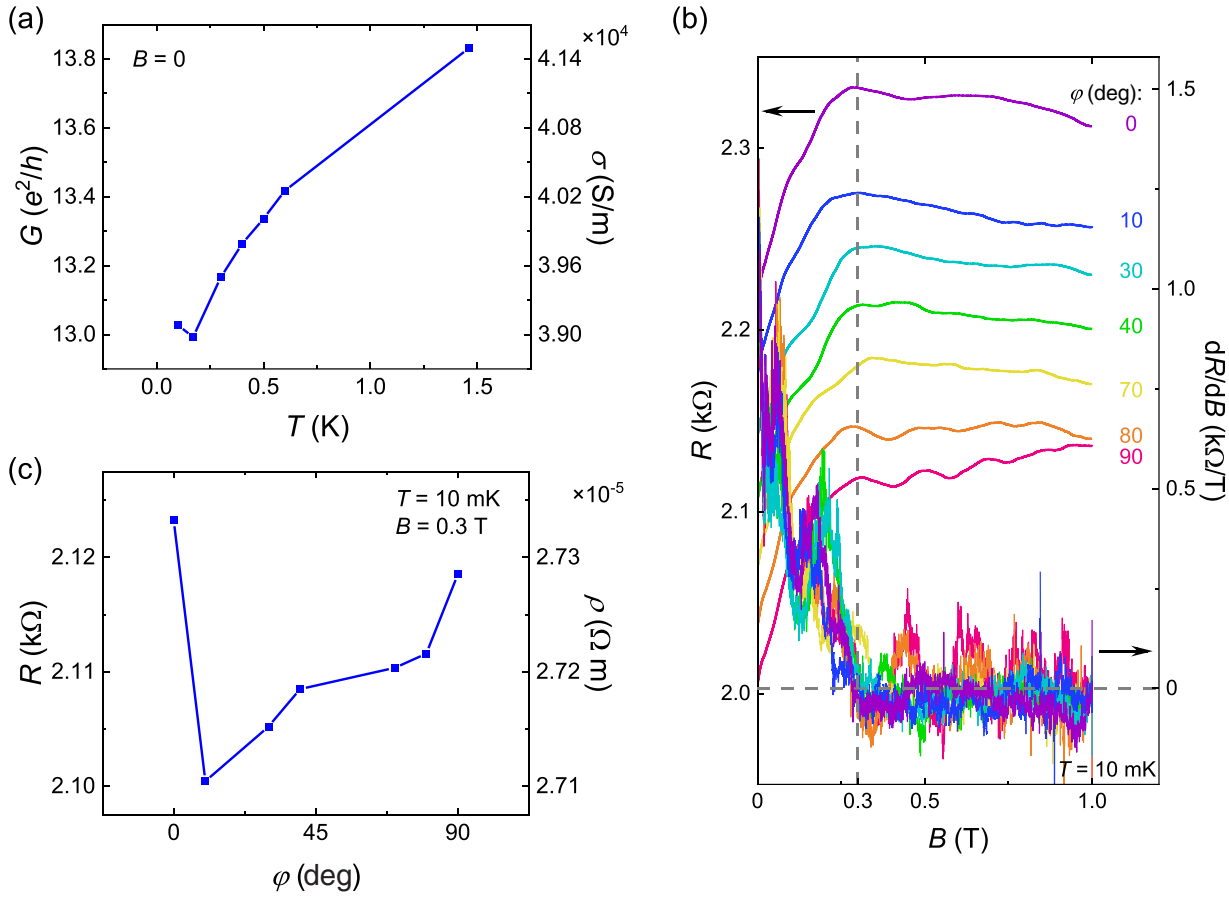

FIG. 7. Zero-field conductance and full range MR of junction 1. (a) Conductance $G(B = 0)$ (left axis) and corresponding conductivity $\sigma(B = 0)$ (right axis) at temperatures below 1.5 K. (b) Resistance (left axis) and dR/dB (right axis) versus in-plane magnetic field from 0 to 1 T with different orientations. Resistance traces are shifted for visibility and the specific values are shown in (c). The derivative drops to 0 at approximately 0.3 T. (c) Resistance (left axis) and corresponding resistivity (right axis) under 0.3 T in-plane magnetic field with different orientations.

repeatable in junction 2 (Fig. 5). As shown in Fig. 5(a), periodic MC under B_y is observed at 10 mK. The amplitude is in the same order of magnitude as junction 1. Taking advantage of the FFT technique, a frequency of $4.91\,\mathrm{T}^{-1}$ is obtained in Fig. 5(b), similar to junction 1 ($4.76\,\mathrm{T}^{-1}$). The small frequency difference comes from the slight distinction in the channel length of the two junctions due to the limitation of fabrication accuracy. Within experimental error, the observed frequency is consistent with AAS oscillation, indicating 1D helical edge states flowing along the hinges of $MoTe_2$.

APPENDIX B: MC OSCILLATIONS UNDER B_z FIELD IN JUNCTION 1

MC under out of plane magnetic field B_z is investigated in Fig. 6. After subtracting a smooth background, MC up to 6 T is obtained in Fig. 6(a), which exhibits complex behaviors. The amplitude of the oscillations is $\sim 0.1\,e^2/h$, several times larger than that under the in-plane field [Fig. 4(a)]. Here we discuss the possible origins of the oscillations under the B_z field. Applying FFT, the major peak locates at $0.38\,\mathrm{T}^{-1}$, corresponding to a period of 2.6 T [Fig. 6(b)]. If we translate this value into area considering the AAS interference, the calculated area ($\sim 10^{-3}\,\mu\mathrm{m}^2$) is three orders of magnitude smaller than the actual area ($\sim 3\,\mu\mathrm{m}^2$), which rules out the origination from the edge interference. The aperiodic oscillations and FFT spectrum are reminiscent of universal conductance fluctuations (UCFs), which may originate from the transport of the top and bottom surface states. We also consider the possibility of Shubnikov–de Haas (SdH) oscillations. Conductance versus $1/B_z$ and its FFT spectrum is shown in Figs. 6(c) and 6(d), respectively. From this data, we could not exclude SdH oscillations as a possible origin, though the magnetic field applied here is quite small to observe the SdH effect in usual cases. The exact origin of the out of plane oscillations needs further investigation.

APPENDIX C: ZERO-FIELD CONDUCTANCE AND CRITERION FOR REFERENCE POINT IN NMR ANALYSIS

In Fig. 2, ΔG under the B_z field is studied after subtracting the zero-field value $G(B = 0)$, which is shown in Fig. 7(a). Under 1.5 K, $G(B = 0)$ is about $13.5\,e^2/h$ and decreases as the temperature goes down. The corresponding conductivity σ is calculated as $GL/(Wt)$ and shown on the right axis, where

$L = 1.3\,\mu\text{m}$, $W = 2.4\,\mu\text{m}$, and $t = 7$ nm are the corresponding length, width, and thickness of the channel, respectively.

In Fig. 3, we study the MR with an in-plane magnetic field with different orientation angles. A resistance dip near zero magnetic field is found [Fig. 7(b)], which is attributed primarily to the WAL effect. However, under a higher magnetic field, we find the signature of decreasing resistance for all the in-plane fields except $\varphi = 90°$, i.e., the perpendicular one, which is consistent with the chiral anomaly mechanism in Weyl semimetals. The competition between WAL and chiral anomaly results in a nonmonotonic *R*-*B* behavior. To highlight and focus on the field orientation dependent chiral anomaly phenomena, in Fig. 3(b) we show the *R*-*B* curves outside the WAL-dominating region, not starting from 0 T. The criterion for choosing the reference of $R(B = 0.3\,\text{T})$ is the boundary of the resistance dip region with derivative $dR/dB|_{0.3\,\text{T}} = 0$, as shown in Fig. 7(b). The resistance at 0.3 T is exhibited in Fig. 7(c), which is around 2.11 kΩ under 0.3 T in-plane magnetic field. On the right axis, we present the resistivity $\rho = RWt/L$.

[1] Q. H. Wang, K. Kalantar-Zadeh, A. Kis, J. N. Coleman, and M. S. Strano, Electronics and optoelectronics of two-dimensional transition metal dichalcogenides, Nat. Nanotechnol. **7**, 699 (2012).

[2] K. F. Mak and J. Shan, Photonics and optoelectronics of 2D semiconductor transition metal dichalcogenides, Nat. Photonics **10**, 216 (2016).

[3] K. S. Novoselov, A. Mishchenko, A. Carvalho, and A. H. Castro Neto, 2D materials and van der Waals heterostructures, Science **353**, aac9439 (2016).

[4] S. Manzeli, D. Ovchinnikov, D. Pasquier, O. V. Yazyev, and A. Kis, 2D transition metal dichalcogenides, Nat. Rev. Mater. **2**, 17033 (2017).

[5] X. Qian, J. Liu, L. Fu, and J. Li, Quantum spin Hall effect in two-dimensional transition metal dichalcogenides, Science **346**, 1344 (2014).

[6] Y. Sun, S.-C. Wu, M. N. Ali, C. Felser, and B. Yan, Prediction of Weyl semimetal in orthorhombic $MoTe_2$, Phys. Rev. B **92**, 161107 (2015).

[7] A. A. Soluyanov, D. Gresch, Z. Wang, Q. Wu, M. Troyer, X. Dai, and B. A. Bernevig, Type-II Weyl semimetals, Nature (London) **527**, 495 (2015).

[8] Z. Wang, D. Gresch, A. A. Soluyanov, W. Xie, S. Kushwaha, X. Dai, M. Troyer, R. J. Cava, and B. A. Bernevig, $MoTe_2$: A Type-II Weyl Topological Metal, Phys. Rev. Lett. **117**, 056805 (2016).

[9] L. Fu, C. L. Kane, and E. J. Mele, Topological Insulators in Three Dimensions, Phys. Rev. Lett. **98**, 106803 (2007).

[10] L. Fu and C. L. Kane, Topological insulators with inversion symmetry, Phys. Rev. B **76**, 045302 (2007).

[11] J. Zak, Band representations and symmetry types of bands in solids, Phys. Rev. B **23**, 2824 (1981).

[12] J. Cano, B. Bradlyn, Z. Wang, L. Elcoro, M. G. Vergniory, C. Felser, M. I. Aroyo, and B. A. Bernevig, Topology of Disconnected Elementary Band Representations, Phys. Rev. Lett. **120**, 266401 (2018).

[13] H. C. Po, A. Vishwanath, and H. Watanabe, Symmetry-based indicators of band topology in the 230 space groups, Nat. Commun. **8**, 50 (2017).

[14] F. Schindler, M. Cook Ashley, G. Vergniory Maia, Z. Wang, S. P. Parkin Stuart, B. A. Bernevig, and T. Neupert, Higher-order topological insulators, Sci. Adv. **4**, eaat0346 (2018).

[15] E. Khalaf, H. C. Po, A. Vishwanath, and H. Watanabe, Symmetry Indicators and Anomalous Surface States of Topological Crystalline Insulators, Phys. Rev. X **8**, 031070 (2018).

[16] Z. Wang, B. J. Wieder, J. Li, B. Yan, and B. A. Bernevig, Higher-Order Topology, Monopole Nodal Lines, and the Origin of Large Fermi Arcs in Transition Metal Dichalcogenides XTe_2 (X = Mo, W), Phys. Rev. Lett. **123**, 186401 (2019).

[17] M. Ezawa, Second-order topological insulators and loop-nodal semimetals in transition metal dichalcogenides XTe_2 (X = Mo, W), Sci. Rep. **9**, 5286 (2019).

[18] F. Tang, H. C. Po, A. Vishwanath, and X. Wan, Efficient topological materials discovery using symmetry indicators, Nat. Phys. **15**, 470 (2019).

[19] W. D. Wang, S. Kim, M. H. Liu, F. A. Cevallos, R. J. Cava, and N. P. Ong, Evidence for an edge supercurrent in the Weyl superconductor $MoTe_2$, Science **368**, 534 (2020).

[20] A. Bachtold, C. Strunk, J. P. Salvetat, J. M. Bonard, L. Forro, T. Nussbaumer, and C. Schonenberger, Aharonov-Bohm oscillations in carbon nanotubes, Nature (London) **397**, 673 (1999).

[21] H. Peng, K. Lai, D. Kong, S. Meister, Y. Chen, X.-L. Qi, S.-C. Zhang, Z.-X. Shen, and Y. Cui, Aharonov–Bohm interference in topological insulator nanoribbons, Nat. Mater. **9**, 225 (2010).

[22] J. H. Bardarson, P. W. Brouwer, and J. E. Moore, Aharonov-Bohm Oscillations in Disordered Topological Insulator Nanowires, Phys. Rev. Lett. **105**, 156803 (2010).

[23] Y. Zhang and A. Vishwanath, Anomalous Aharonov-Bohm Conductance Oscillations from Topological Insulator Surface States, Phys. Rev. Lett. **105**, 206601 (2010).

[24] F. Xiu, L. He, Y. Wang, L. Cheng, L.-T. Chang, M. Lang, G. Huang, X. Kou, Y. Zhou, X. Jiang *et al.*, Manipulating surface states in topological insulator nanoribbons, Nat. Nanotechnol. **6**, 216 (2011).

[25] L. X. Wang, C. Z. Li, D. P. Yu, and Z. M. Liao, Aharonov-Bohm oscillations in Dirac semimetal Cd_3As_2 nanowires, Nat. Commun. **7**, 10769 (2016).

[26] B. C. Lin, S. Wang, L. X. Wang, C. Z. Li, J. G. Li, D. P. Yu, and Z. M. Liao, Gate-tuned Aharonov-Bohm interference of surface states in a quasiballistic Dirac semimetal nanowire, Phys. Rev. B **95**, 235436 (2017).

[27] J. H. Bardarson and J. E. Moore, Quantum interference and Aharonov-Bohm oscillations in topological insulators, Rep. Prog. Phys. **76**, 056501 (2013).

[28] Y. Aharonov and D. Bohm, Significance of electromagnetic potentials in the quantum theory, Phys. Rev. **115**, 485 (1959).

[29] K. Luo, H. Geng, L. Sheng, W. Chen, and D. Y. Xing, Aharonov-Bohm effect in three-dimensional higher-order topological insulators, Phys. Rev. B **104**, 085427 (2021).

[30] H. B. Nielsen and M. Ninomiya, The Adler-Bell-Jackiw anomaly and Weyl fermions in a crystal, Phys. Lett. B **130**, 389 (1983).

[31] S. Matsuo, T. Koyama, K. Shimamura, T. Arakawa, Y. Nishihara, D. Chiba, K. Kobayashi, T. Ono, C.-Z. Chang, K. He *et al.*, Weak antilocalization and conductance fluctuation in a submicrometer-sized wire of epitaxial Bi_2Se_3, Phys. Rev. B **85**, 075440 (2012).

[32] B. Hamdou, J. Gooth, A. Dorn, E. Pippel, and K. Nielsch, Aharonov-Bohm oscillations and weak antilocalization in topological insulator Sb_2Te_3 nanowires, Appl. Phys. Lett. **102**, 223110 (2013).

[33] L. A. Jauregui, M. T. Pettes, L. P. Rokhinson, L. Shi, and Y. P. Chen, Magnetic field-induced helical mode and topological transitions in a topological insulator nanoribbon, Nat. Nanotechnol. **11**, 345 (2016).

[34] H. Yuan, M. S. Bahramy, K. Morimoto, S. Wu, K. Nomura, B.-J. Yang, H. Shimotani, R. Suzuki, M. Toh, C. Kloc *et al.*, Zeeman-type spin splitting controlled by an electric field, Nat. Phys. **9**, 563 (2013).

[35] C. H. Naylor, W. M. Parkin, J. L. Ping, Z. L. Gao, Y. R. Zhou, Y. Kim, F. Streller, R. W. Carpick, A. M. Rappe, M. Drndic *et al.*, Monolayer single-crystal 1T′-$MoTe_2$ grown by chemical vapor deposition exhibits weak antilocalization effect, Nano Lett. **16**, 4297 (2016).

[36] D. H. Keum, S. Cho, J. H. Kim, D. H. Choe, H. J. Sung, M. Kan, H. Kang, J. Y. Hwang, S. W. Kim, H. Yang *et al.*, Bandgap opening in few-layered monoclinic $MoTe_2$, Nat. Phys. **11**, 482 (2015).

[37] S. Hikami, A. I. Larkin, and Y. Nagaoka, Spin-orbit interaction and magnetoresistance in the two dimensional random system, Prog. Theor. Phys. **63**, 707 (1980).

[38] L.-X. Qin, X.-C. Pan, F.-Q. Song, L. Zhang, Z.-H. Sun, M.-Q. Li, P. Gao, B.-C. Lin, S.-M. Huang, R. Zhu *et al.*, Confined-path interference suppressed quantum correction on weak antilocalization effect in a $BiSbTeSe_2$ topological insulator, Appl. Phys. Lett. **112**, 032102 (2018).

[39] Y. P. Qi, P. G. Naumov, M. N. Ali, C. R. Rajamathi, W. Schnelle, O. Barkalov, M. Hanfland, S. C. Wu, C. Shekhar, Y. Sun *et al.*, Superconductivity in Weyl semimetal candidate $MoTe_2$, Nat. Commun. **7**, 11038 (2016).

[40] S. A. Parameswaran, T. Grover, D. A. Abanin, D. A. Pesin, and A. Vishwanath, Probing the Chiral Anomaly with Nonlocal Transport in Three-Dimensional Topological Semimetals, Phys. Rev. X **4**, 031035 (2014).

[41] X. Huang, L. Zhao, Y. Long, P. Wang, D. Chen, Z. Yang, H. Liang, M. Xue, H. Weng, Z. Fang *et al.*, Observation of the Chiral-Anomaly-Induced Negative Magnetoresistance in 3D Weyl Semimetal TaAs, Phys. Rev. X **5**, 031023 (2015).

[42] X. Luo, F. C. Chen, J. L. Zhang, Q. L. Pei, G. T. Lin, W. J. Lu, Y. Y. Han, C. Y. Xi, W. H. Song, and Y. P. Sun, T_d-$MoTe_2$: A possible topological superconductor, Appl. Phys. Lett. **109**, 102601 (2016).

[43] S. Cho, B. Dellabetta, R. D. Zhong, J. Schneeloch, T. S. Liu, G. D. Gu, M. J. Gilbert, and N. Mason, Aharonov-Bohm oscillations in a quasi-ballistic three-dimensional topological insulator nanowire, Nat. Commun. **6**, 7634 (2015).

[44] J. Dufouleur, L. Veyrat, A. Teichgräber, S. Neuhaus, C. Nowka, S. Hampel, J. Cayssol, J. Schumann, B. Eichler, O. G. Schmidt *et al.*, Quasiballistic Transport of Dirac Fermions in a Bi_2Se_3 Nanowire, Phys. Rev. Lett. **110**, 186806 (2013).

[45] S. Washburn, C. P. Umbach, R. B. Laibowitz, and R. A. Webb, Temperature dependence of the normal-metal Aharonov-Bohm effect, Phys. Rev. B **32**, 4789 (1985).

[46] S. S. Hong, Y. Zhang, J. J. Cha, X. L. Qi, and Y. Cui, One-dimensional helical transport in topological insulator nanowire interferometers, Nano Lett. **14**, 2815 (2014).